Supporting Information

Experimental Section

All chemicals used in this study were analytical grade and used without further purification.

Synthesis of HCCM

Resorcinol (0.1 g) and cetyltrimethyl ammonium bromide (CTAB 0.2 g) were added into the mixed solution including deionized water (25mL), ethanol (15mL) and ammonia solution with stirring for 30 min. After that, tetraethyl orthosilicate and formaldehyde solution (0.58 mL, 37 wt %) were added and continuously stirred for 15h at 40°C. Then, the red solution was poured into Teflon-lined autoclave with 50 mL and maintained at 100 °C for 24 h. The products were washed and dried at 60 °C. Subsequently the products were annealed under flowing Ar at 900 °C for 2 h to form HCCM-SiO_2. Finally, SiO_2 was etched at room temperature for 6h in 2 M KOH solution to obtain HCCMS.

Synthesis of GO and N-RGO

According to the modified Hummer method, we prepared RGO the graphite oxide (GO) sheets were peeled from natural graphite powder (99.9995%, 325 mesh) with the following several steps [1]. At first, 180 mL of H_2SO_4 (98%) and 20mL of H_3PO_4 (85%) were evenly mixed in a 500 mL beaker to form a homogeneous acid solution. Then, the solution was slowly poured into another 500 ml beaker with the graphite power inside together with magnetic stirring at 50 °C. *After that, t*he appropriate amount of $KMnO_4$ was slowly added to the mixed solution followed by 60-minute stirring. In this process, the solution temperature should be kept constant (at 50 °C). A certain concentration of H_2O_2 solution was slowly dropped into solution and again the mixture was stirred for 3h at 50°C, and then cooled to room temperature naturally. The final precipitation was collected by centrifugal separation and washing with deionized water several times. The precipitation was desiccated at 60 °C for 24h until the solid product (graphene oxide, GO) was reached. Hydrothermal reduction method at high temperature was also employed to get the reduced graphene oxide (RGO). Furthermore, 0.2 g of synthesized GO powder and melamine are mixed and ground evenly with following thermal treatment at 900 °C (5°C min^{-1}) for 1 h under flowing Ar to obtain N-RGO.

Preparation of HCCMS/Fe_3O_4

0.15g black HCCMS powders was added into 30 mL $Fe(NO_3)_3$ aqueous solution (0.15 M) followed by continuously stirring for 12 h. Then, the sample was collected, washed and dried. Subsequently, the products were annealed under flowing Ar at 900 °C for 2 h to form HCCMS/Fe_3O_4.

Preparation of HCCMS/Fe_3O_4@RGO and HCCMS/Fe_3O_4@N-RGO

0.15g HCCMS black powders were added into the mixed solution of $Fe(NO_3)_3$ and GO followed by continuously stirring for 12 h. The final sample was collected and annealed to form HCCMS/Fe_3O_4@RGO. HCCMS/Fe_3O_4@RGO was then mixed with melamine (mass ratio 1:20), with following thermal treatment at 900 °C (5°C min^{-1}) for 1 h under flowing Ar to obtain HCCMS/Fe_3O_4@N-RGO.

Characterization and measurements

Cyclic voltammetry (CV) curves were performed at a scan rate of 25mV•s-1in a supporting electrolyte consisting of 10mM LiI, 1mM I_2, and 100mM $LiClO_4$ in acetonitrile and carried out in a three-electrode system. Pt thin film was used as the CE, and Ag/AgCl was used as the reference electrode. Electrochemical impedance spectroscopy (EIS) of symmetrical cells was recorded in a frequency range of 0.01∼10^6 Hz and at alternating current amplitude of 10 mV. Tafel polarization measurements were also performed in a symmetrical cell and kept stationary conditions with the voltage range −1 to 1 V at a scan rate of 50 mV/s. Photovoltaic measurements of photocurrent density−voltage ($J-V$) curves were measured by a solar light simulator under an illumination of 100 mW·cm^{-2}, AM 1.5 and using a digital source meter (Keithley 2410). The filling factor (*FF*) and the power conversion efficiency (*PCE*) of the DSSC were calculated according to the following equations. All the measurements were performed at room temperature.

$$PCE = \frac{J_{max} \times V_{max}}{P_{in}} \times \frac{J_{SC} \times V_{OC} \times FF}{P_{in}} \times 100\% \quad , \qquad (1)$$

$$FF = \frac{J_{max} \times V_{max}}{J_{sc} \times V_{oc}}, \quad (2)$$

in which, J_{sc} is the short-circuit current density (mA·cm^{-2}), V_{oc} is the open-circuit voltage (V), P_{in} is the incident light power and J_{max} (mA·cm^{-2}) and V_{max}(V) are the current density and voltage at the point of maximum power output in the J-V curve respectively.

The surface morphology and microstructures of CEs was observed via a field-emission scanning electron microscopy (JSM-6701F, JEOL accelerating voltage of 5 kV) and a high-resolution transmission electron microscopy (HRTEM, JEOL-2010, operating voltage of 200 kV). All samples were prepared by depositing a drop of diluted suspensions in ethanol on a carbon-film-coated copper grid. The crystalline structures of Fe_3O_4 and Fe_3O_4@3DRGO powders were recorded via Raman spectroscopy and a Rigaku/Max-3A X-ray diffractometer with Cu Kα radiation (λ = 1.54178 Å). X-ray photoelectron spectra were conducted using a SmartLab 9KW to study the chemical states.

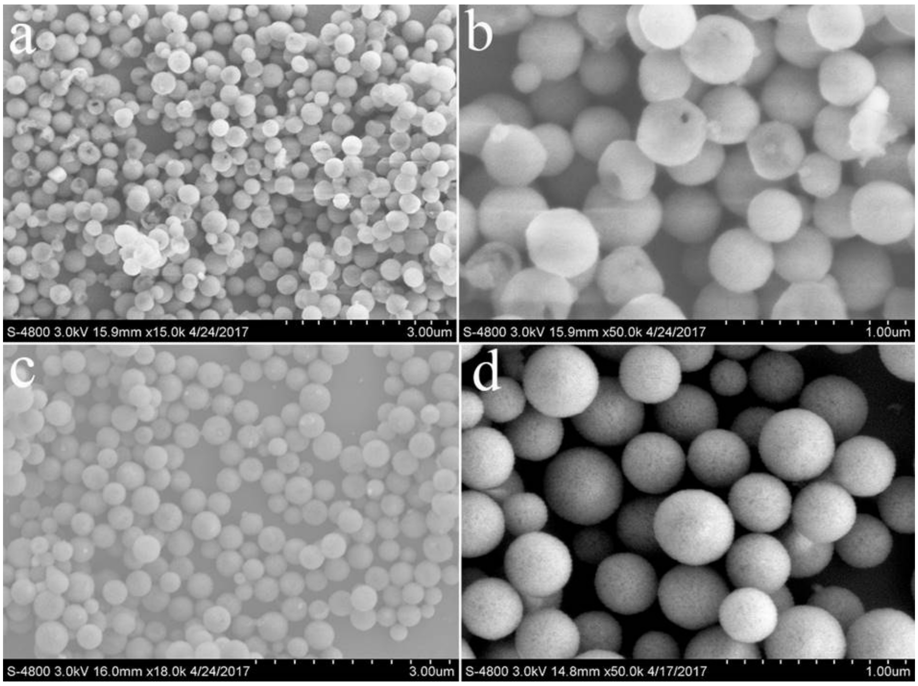

Fig S1 a and b SEM images of the carbon microspheres before the annealing in different amplification scales. c and d the carbon microspheres after the annealing in different amplification scales

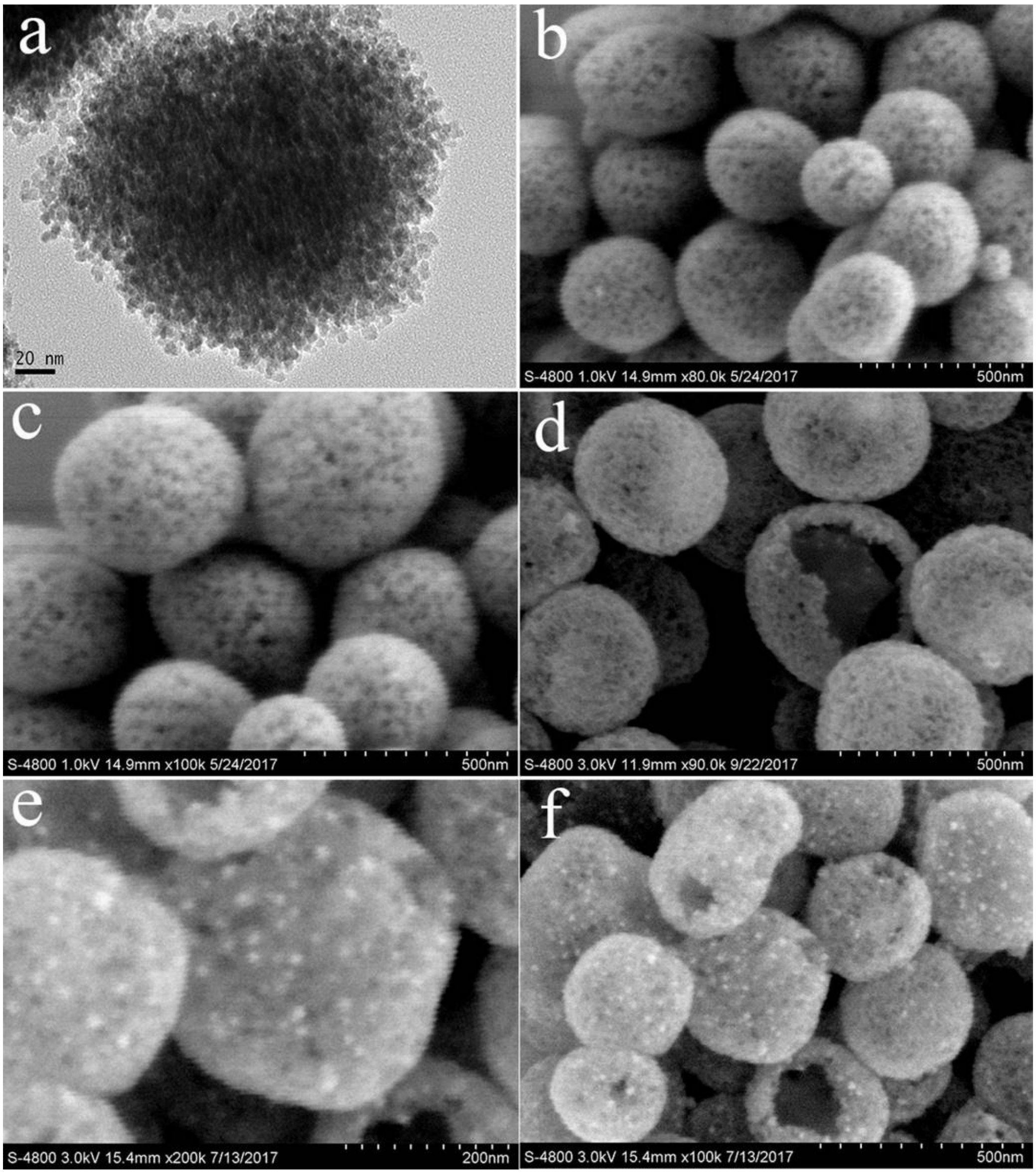

Fig S 2. (a) the agglomeration of Fe_3O_4 nanoparticles, (b) (c) and (d) HCCM has been formed. (e) and (f) Fe_3O_4 nanoparticles were forced into the mesoporous.

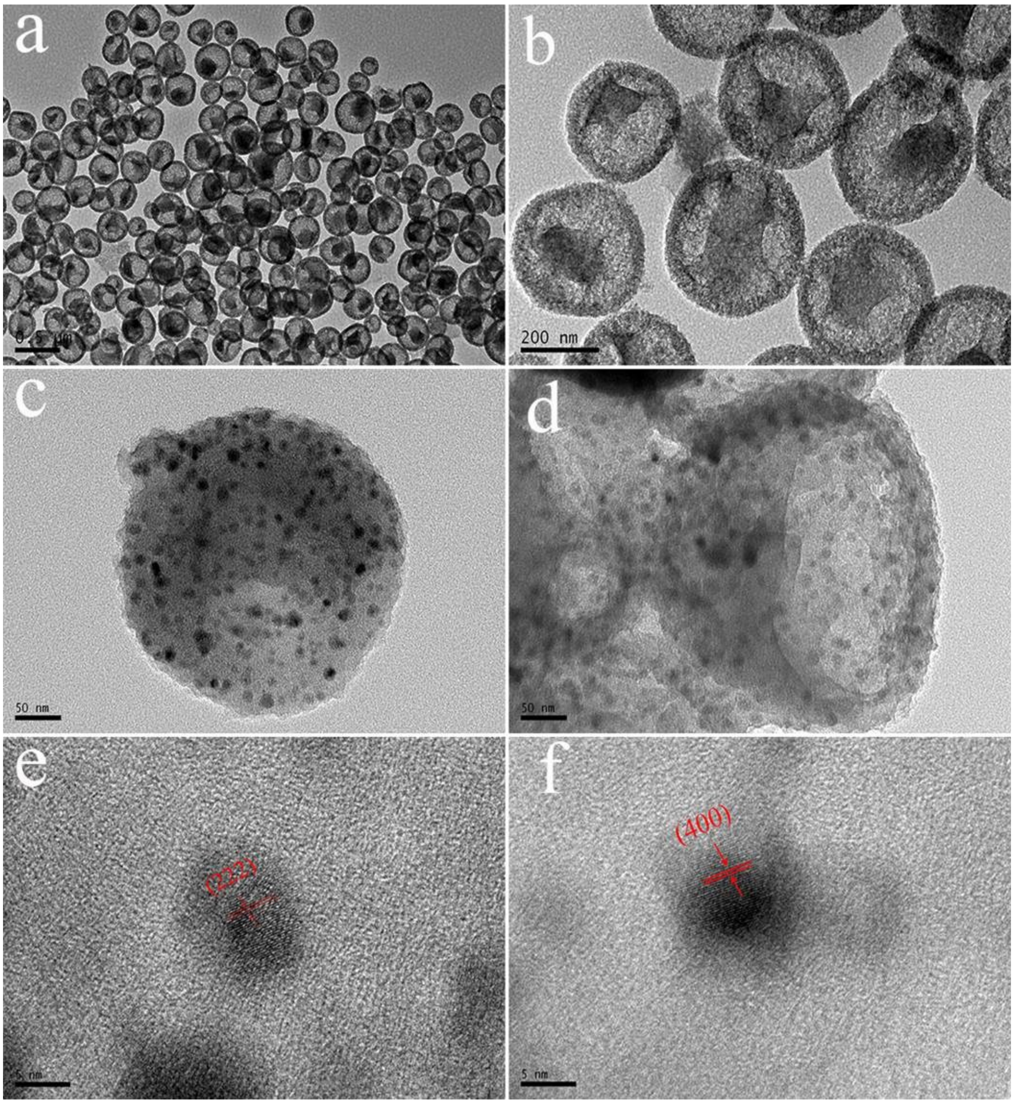

Fig S 3. (a) and (b) HCCM is displayed by TEM, (c) and (d) Fe_3O_4/HCCM, (e) and (f) HRTEM images of Fe_3O_4 nanoparticles in mesoporous.

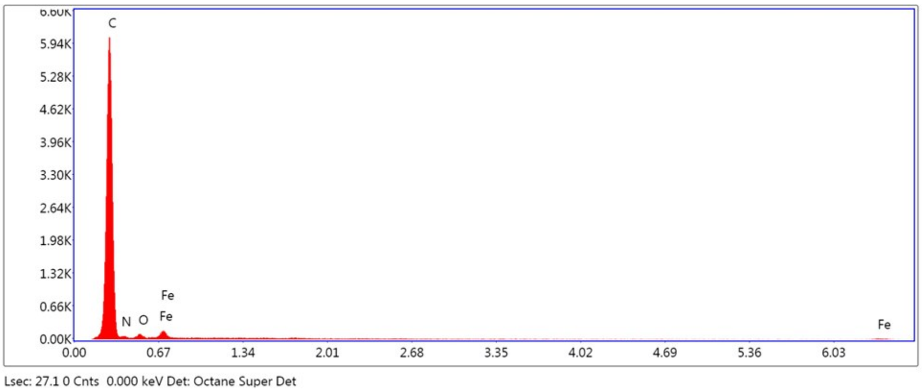

Fig S 4. N, O, C and Fe were clearly analyzed by EDS.

The formation of the hollow structure of Fe_3O_4 nanoparticles in the composite materials are expanded and distributed uniformly in the mesoporous carbon spheres from inside to outside, and this may decrease the clarity of flake-shaped core, as shown in Fig. 3b and Fig. 3d of the manuscript. To prove this, we changed the stirring time of the composite materials to 6 hours and checked their TEM images in comparison to the ones stirred for 12 hours (HCCMS/Fe_3O_4@RGO and HCCMS/Fe_3O_4@N-RGO in the manuscript in the manuscript). It is found that the Fe_3O_4 nanoparticles with 6 hours stirring are not fully penetrated into the mesoporous holes of carbon spheres, and the flake-shaped core can be observed, indicated by red arrows in the figure below. Furthermore, because of the introduction of graphene encapsulating HCCMS/Fe_3O_4, the composite sphere is thickened, which will again affect the clarity of flake-shaped core in TEM images.

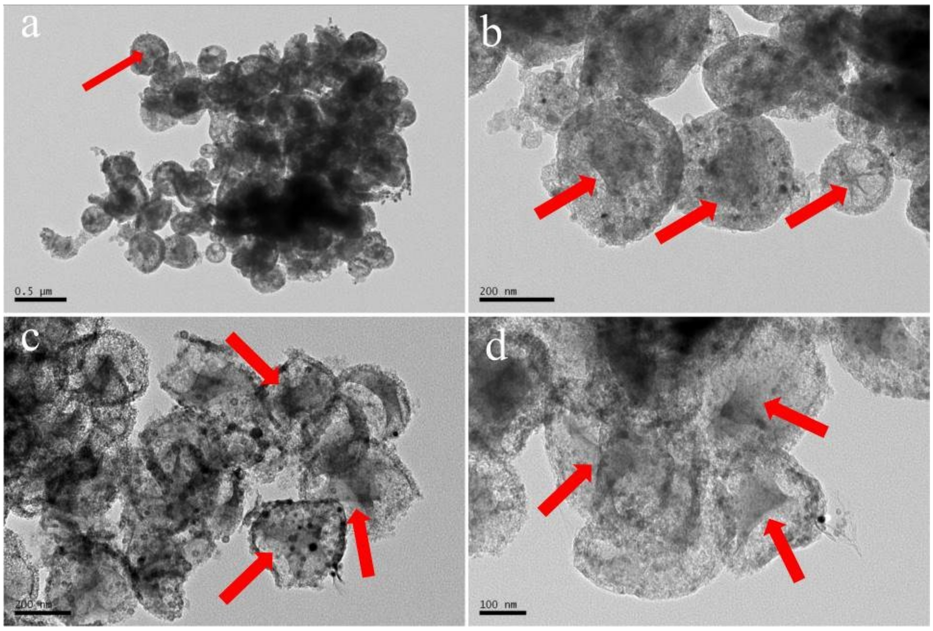

Fig S 5. TEM images of composite spheres that are stirred for 6 hours: (a) and (b) HCCMS/Fe_3O_4@RGO, (c) and (d) HCCMS/Fe_3O_4@N-RGO. It is found that the composite materials with shorter stirring time, the flake-shaped core can be observed due to the incomplete penetration of Fe_3O_4 nanoparticles into the mesoporous holes of carbon sphere.

In addition, in order to explain the appearance of the flake-shaped core, TEM images of the unprocessed carbon spheres were recorded. It is found that the spheres are solid, presented in figure below (a and b). A small amount of rigid silicate in the core shrinks sharply due to the dehydrogenation of resin polymer after high temperature annealing treatment. In this process, the nuclear contraction is irregular, thus forming flake-shaped core (c and d). H Wang et al (ACS Applied Materials & Interfaces, 2017, 9(12): 10610-10617.) reported hollow nitrogen-doped carbon spheres with Fe_3O_4 nanoparticles encapsulated as a highly active oxygen-reduction catalyst and they found a sphere-shaped core inside. In ours a flake-shaped core forms inside. This may be due to different processing conditions.

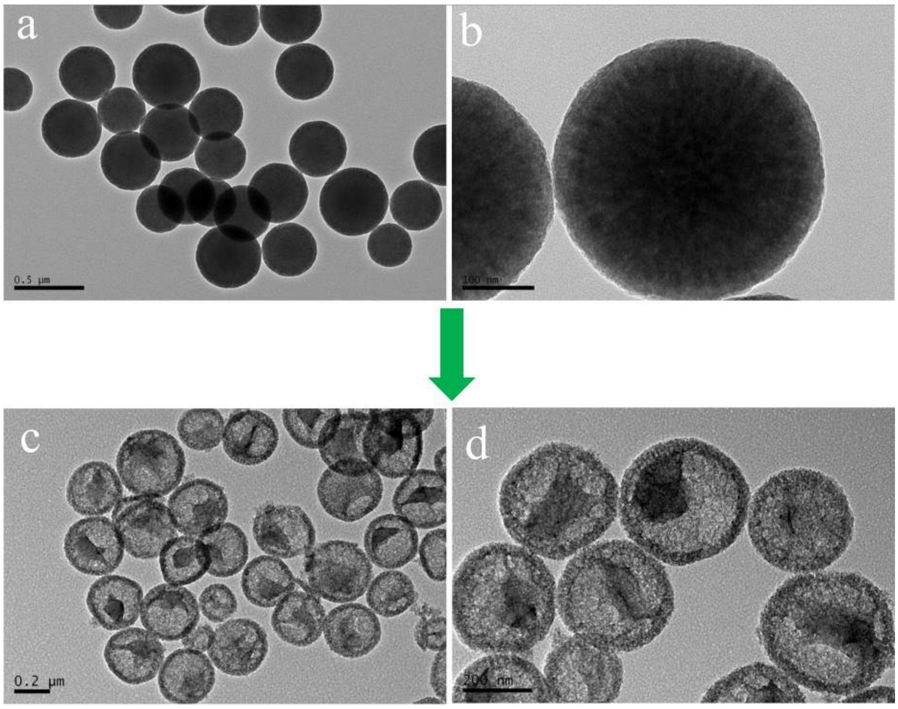

Fig S 6. (a) and (b) the unprocessed carbon spheres. (c) and (d) carbon spheres after annealing.

We think the large size particles are Fe_3O_4. If they were carbon materials, they must be recorded in XRD patterns. If they were solids other than Fe_3O_4, their XRD peaks must be recorded too. However, in the XRD patterns, there are only peaks of Fe_3O_4. A few Fe_3O_4 nanoparticles did not enter mesoporous holes during the synthesis process, which would form larger nanoparticles outside the carbon sphere or between the interfaces of microspheres without the confinement of the spheres. Moreover, we synthesized samples HCCMS/Fe_3O_4@RGO and HCCMS/Fe_3O_4@N-RGO again with the same conditions and checked their TEM images, shown as c and d in the figure below. The large particles are circled in red. In order to make a comparison, we also showed the samples HCCMS/Fe_3O_4@RGO (a) and HCCMS/Fe_3O_4@N-RGO (b). The corresponding explanation is added to the Support Information.

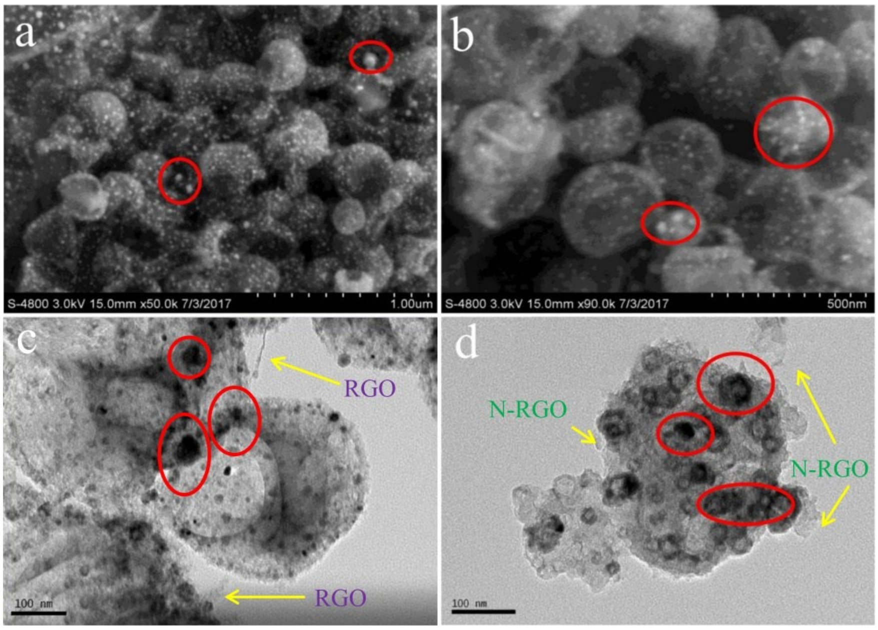

Fig S 7. (a) and (c) SEM and TEM images of samples HCCMS/Fe_3O_4@RGO. (b) and (d) SEM and TEM images of samples of HCCMS/Fe_3O_4@N-RGO. The samples HCCMS/Fe_3O_4@RGO (c) and HCCMS/Fe_3O_4@N-RGO synthesized again with the same conditions to the manuscript. The large particles are circled in red.

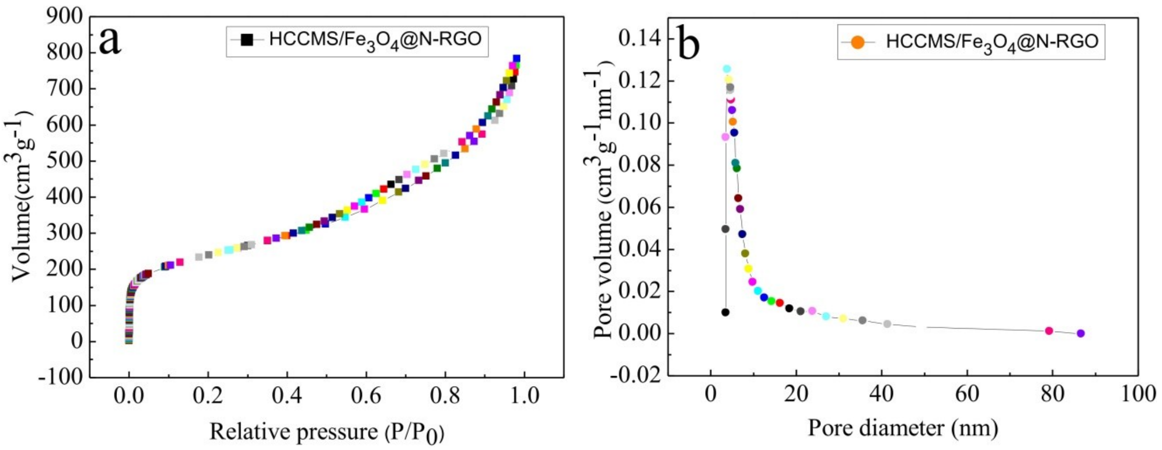

Fig S8. (a) Brunauer−Emmett−Teller (BET) analysis clearly revealed that a specific surface area is about 850 $m^2 \cdot g^{-1}$ for HCCMS/Fe_3O_4@N-RGO. (b) the BJH revealed that the pore size distribution is about 5.86 nm

Composition analysis of RGO and N-RGO

The surface composite of RGO and N-RGO are further investigated by XPS test. The survey scan spectrum (Figure S1) reveals the existence of C, N, O in N-RGO and comparing to RGO.

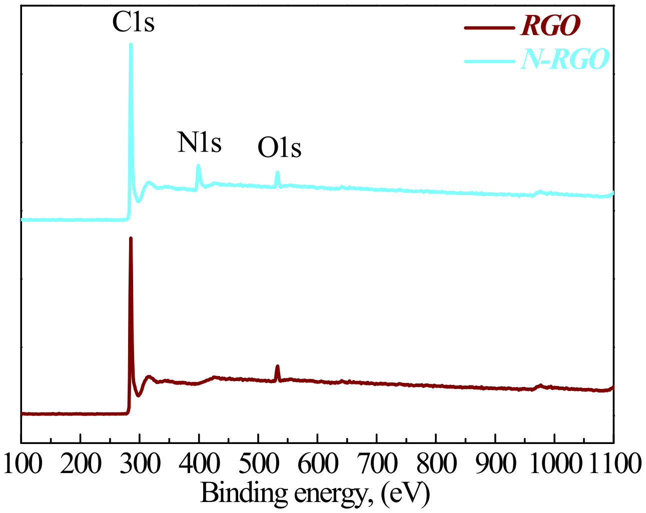

Fig S9. XPS full spectrum of RGO and N-RGO.

Electrochemical part calculation

The E_{pp} value of N-RGO (0.26 V) is significantly smaller than that of Pt (0.34 V) and RGO (0.37 V), further demonstrating that the N doping is in favor of the enhanced catalytic activity toward reduction of I_3^- [2, 3].

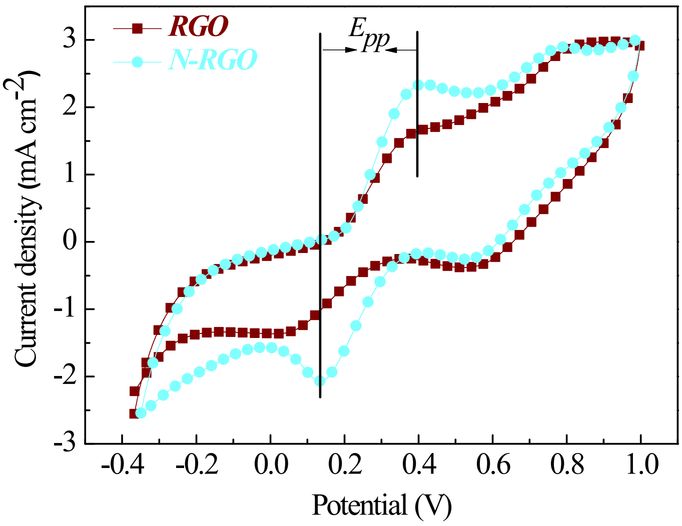

Fig S10. CV curves of iodide/triiodide redox species for RGO and N-RGO at a scan rate of 25 mV/s.

Tafel polarization is influential electrochemical characterization method to examine catalytic activity for reducing I_3^- and diffusion coefficient of I_3^- [4, 5]. N-RGO owned the better catalytic activities more than RGO CEs.

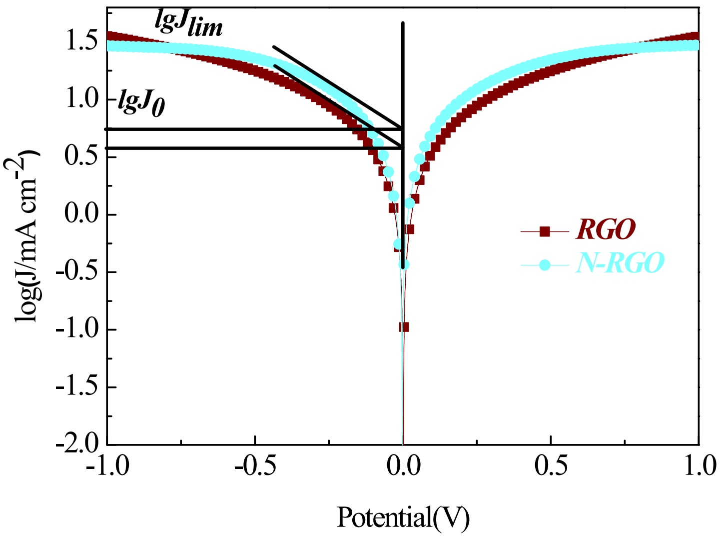

Fig S11. Tafel polarization curves of symmetrical cells of RGO and N-RGO for I^-/ I_3^-.

Electrochemical impedance spectroscopy (*EIS*) is tested to assess the catalytic activities and charge-transfer abilities of RGO and N-RGO on the reduction of triiodide [6, 7]. N-RGO CE had better catalytic activities and charge-transfer abilities than RGO, and be close to Pt, which is shown in Fig 4a.

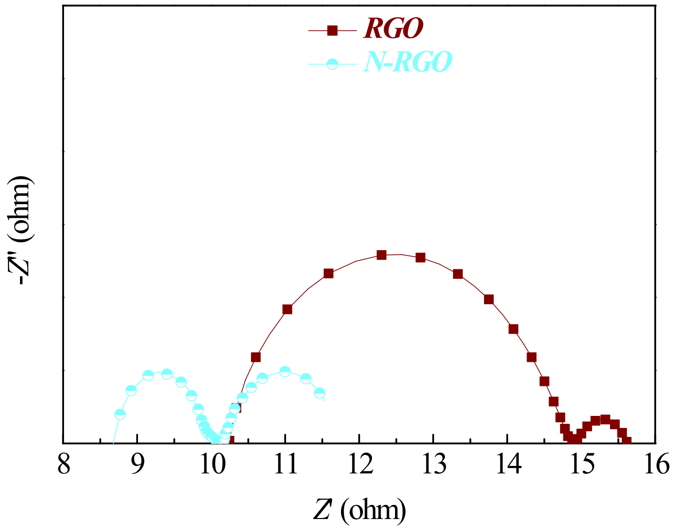

Fig S12. Electrochemical impedance spectroscopy (*EIS*) is tested to assess RGO and N-RGO.

The layered structure of graphene contributes to accelerate electronic movement. However, the structure of graphene is relatively stable, which lead to cannot being the oxidation and reduction of I^-/I_3^- quickly [8, 9]. N species are introduced to embellish graphene, in which providing more active sites to enhance the catalytic activity of CE. *J–V* curves were tested to assess directly photoelectric conversion efficiency of RGO and N-RGO. The photoelectric conversion efficiency of N-RGO is 7.66% and similar to Pt's value (7.49%).

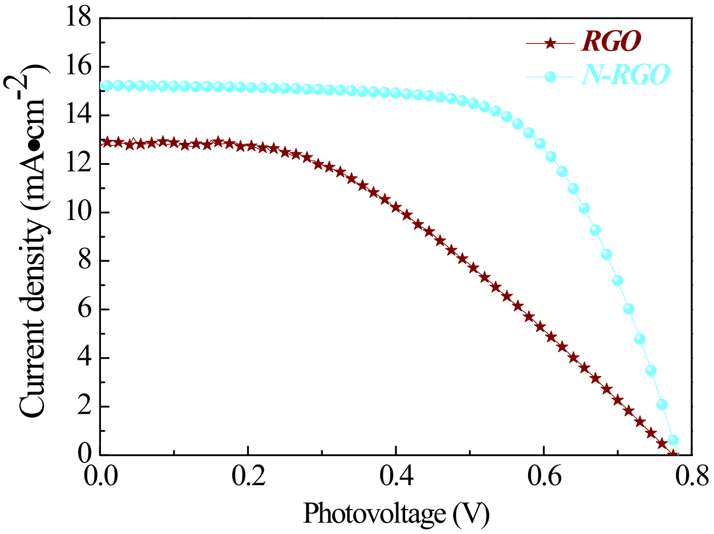

Fig S13. a Schematic diagram about the work principle of DSSC. b The working schematic diagram is that RGO and N-RGO are used as CE. c *J–V* curves of RGO and N-RGO.

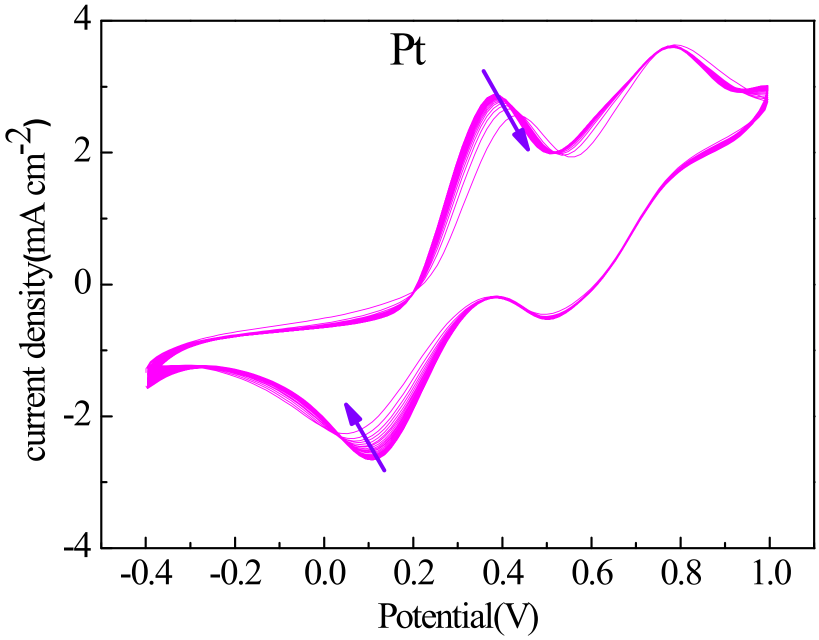

Fig S14. 60-cycle CV curves of Pt with a 25mV/s scanning speed.

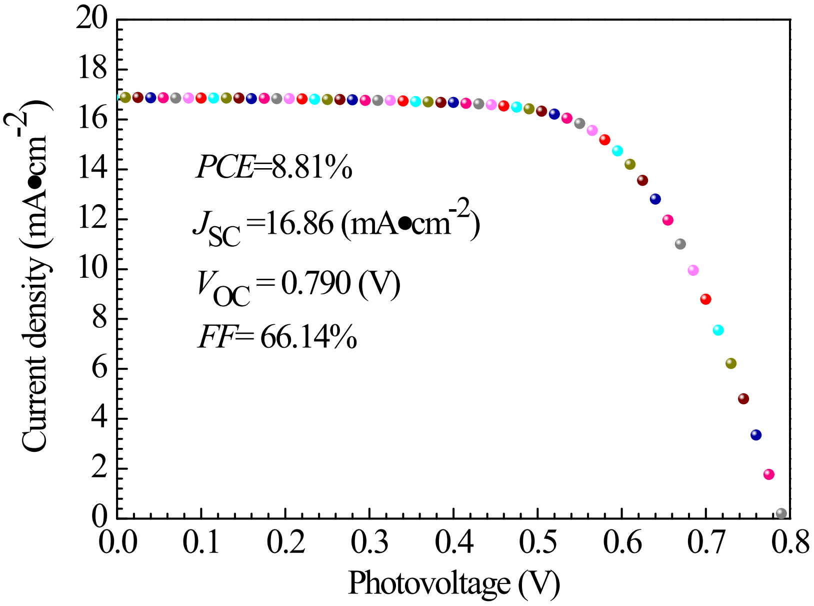

Fig S15. *J–V* curves were carried out again, after 60-cycle CV curves for HCCMS/Fe_3O_4@N-RGO.

Reference

[1] J. Y. Kim, W. H. Lee, J. W. Suk, J. R. Potts, H. Chou, I. N. Kholmanov, R. D. Piner, J. Lee, D. Akinwande, R. S. Ruoff, Advance Materials. 25 (2013), pp. 2308-2313.

[2] X. Zhang, Y. Yang, S. Guo, et al. ACS applied materials & interfaces, 7 (2015), pp. 8457-8464.

[3] X. Zhang, M. Zhen, J. Bai, et al. ACS applied materials & interfaces, 8 (2016), pp. 17187-17193.

[4] Y. Duan, Q. Tang, J. Liu, et al. Angewandte Chemie International Edition, 53 (2014), pp. 14569-14574.

[5] Y. Duan, Q. Tang, B. He, et al. Nanoscale, 6 (2014), pp. 12601-12608.

[6] X. Zhang, M. Zhen, J. Bai, et al. ACS applied materials & interfaces, 8 (2016), pp. 17187-17193.

[7] H. Wang, W. Wei, Y. H. Hu. Journal of Materials Chemistry A, 1 (2013), pp. 6622-6628.

[8] K. Kakiage, Y. Aoyama, T. Yano, et al. Chemical Communications, 51 (2015), pp. 15894-15897.

[9] P. J. Chang, K. Y. Cheng, S. W. Chou, et al. Chemistry of Materials, 28 (2016), pp. 2110-2119.